

Article

Deformation and Related Slip Due to the 2011 Van Earthquake (Turkey) Sequence Imaged by SAR Data and Numerical Modeling

Elisa Trasatti *, Cristiano Tolomei, Giuseppe Pezzo, Simone Atzori and Stefano Salvi

Istituto Nazionale di Geofisica e Vulcanologia, Rome 00143, Italy; cristiano.tolomei@ingv.it (C.T.); giuseppe.pezzo@ingv.it (G.P.); simone.atzori@ingv.it (S.A.); stefano.salvi@ingv.it (S.S.)

* Correspondence: elisa.trasatti@ingv.it; Tel.: +39-06-5186-0349

Academic Editors: Zhenhong Li, Magaly Koch and Prasad S. Thenkabail

Received: 5 February 2016; Accepted: 14 June 2016; Published: 22 June 2016

Abstract: A Mw 7.1 earthquake struck the Eastern Anatolia, near the city of Van (Turkey), on 23 October 2011. We investigated the coseismic surface displacements using the InSAR technique, exploiting adjacent ENVISAT tracks and COSMO-SkyMed images. Multi aperture interferometry was also applied, measuring ground displacements in the azimuth direction. We solved for the fault geometry and mechanism, and we inverted the slip distribution employing a numerical forward model that includes the available regional structural data. Results show a horizontally elongated high slip area (7–9 m) at 12–17 km depth, while the upper part of the fault results unruptured, enhancing its seismogenic potential. We also investigated the post-seismic phase acquiring most of the available COSMO-SkyMed, ENVISAT and TERRASAR-X SAR images. The computed afterslip distributions show that the shallow section of the fault underwent considerable aseismic slip during the early days after the mainshock, of tens of centimeters. Our results support the hypothesis of a seismogenic potential reduction within the first 8–10 km of the fault through the energy release during the post-seismic phase. Despite non-optimal data coverage and coherence issues, we demonstrate that useful information about the Van earthquake could still be retrieved from SAR data through detailed analysis.

Keywords: SAR interferometry; multi aperture interferometry; Van earthquake; remote sensing; numerical modelling; inverse methods; coseismic deformation; post-seismic deformation

1. Introduction

A Mw 7.1 earthquake struck the Eastern Anatolia at 10:41 a.m. on 23 October 2011 (Figure 1). The epicenter was approximately located at 38.76°N, 43.36°E (Turkish Kandilli Observatory and Earthquake Research Institute, KOERI) at a depth of about 16 km, with considerable spatial variations of centroid and aftershocks solutions among different international seismological institutions, of the order of tens of kilometers. The earthquake, located close to the Tabanlı village, about 20 km N-NE the city of Van (about 400,000 inhabitants), caused significant losses and casualties. The focal mechanism indicates an ENE-WSW thrust fault, consistent with the trend observed in eastern Turkey, SW of the Karliova junction along the Arabian plate boundary [1], with an additional minor left-lateral component. The epicenters of the ~1400 $M > 3$ (5300 events $M > 1$) aftershock registered until the end of January 2012 are ~NE-SW aligned. The focal mechanisms of the $M_w > 5$ aftershocks confirm the dominant thrust component (Figure 1) apart from the M 5.1 event of 29 October 2011 which shows a right-lateral strike-slip mechanism. Another earthquake of M_w 5.7 (labeled Edremit-Van earthquake according to KOERI) took place on 9 November 2011. It was located offshore, near the town of Edremit, South of Van, and increased the level of structural damage.

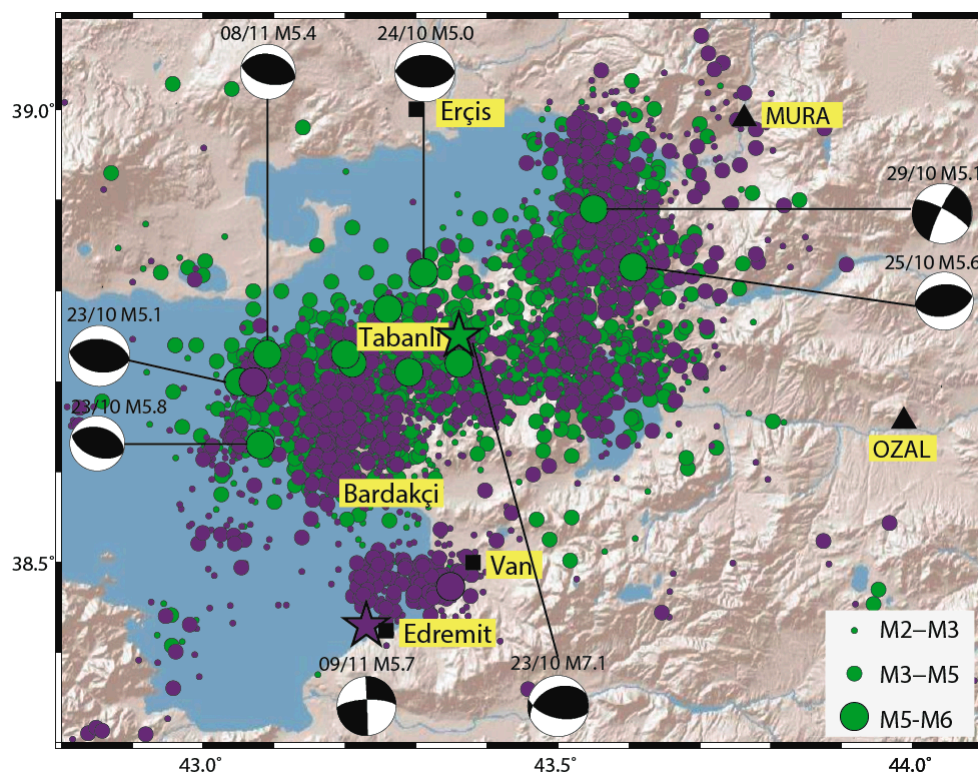


Figure 1. Map of the Mw 7.1 Van earthquake (green star) and related aftershocks until the end of 2011. The Edremit-Van earthquake epicenter is indicated with the purple star. The aftershocks (green before the Edremit-Van earthquake, purple after) are from [2] and KOERI. The available focal mechanisms of $M > 5.0$ events from Global-CMT earthquake catalog and [3] are shown. Near field GPS stations (MURA and OZAL) are indicated by black triangles.

The Van earthquake occurred along a fault that was not previously mapped among the active faults of the region [4], but has been included afterwards [5]. The rupture induced aftershocks on secondary structures, several surface tensional cracks of tens of centimeters, landslides and liquefactions (e.g., [6,7]). Since the length of the surface ruptures does not justify the mainshock magnitude, part of the main fault of the Van earthquake should be considered as blind. Furthermore, along with the main thrust plane, secondary back thrust and left/right lateral fault ruptures occurred [7]. It is not clear whether these fault ruptures are directly connected to the main rupture at depth or not.

Initially, the seismic fault was imaged by [8] in a preliminary seismic data inversion. Results show a maximum slip patch of 4 m at the hypocentral depth (16–20 km), mainly elongated up-dip toward SW. Irmak *et al.* [9] used 35 teleseismic stations to obtain a rupture with bilateral propagation nucleating at greater depths, ~20 km. Other teleseismic inversions described a rupture dominated by failure of a major asperity located up-dip and SW of the hypocenter [10]. The rupture history results indicated above are not in accordance with each other, due to the few seismic recordings in the region and the limited spatial coverage of the seismic stations. The main consequence is a poor estimate of the seismic hazard of the earthquake area. Gallovič *et al.* [11] presented different models to illustrate the broad variability of possible rupture propagation, depending on the unfavorable seismic data constraints. Akinci & Antonioli [12] used a stochastic approach to overcome the described limitations in order to study the characteristics of ground motion. Fielding *et al.* and Elliott *et al.* [3,13] presented two comprehensive studies on the Van earthquake using geodetic, seismological and field observations. The rupture propagated along the dip direction of the fault from the waveform modeling, with two maximum slip zones close and above the hypocenter [3]. The seismological and geodetic inversions both constrain the slip in an area extending about 30 km along strike. Elliott *et al.* [13] used a pair

of an echelon NW, 40° – 54° dipping faults, finding the slip distributed within two separated large concentration zones (one for each fault). Results show the lack of significant slip above 8 km depth, implying a potential future rupture in the shallower part of the faults [3,13–15]. However, GPS data covering 1.5 years after the mainshock to model afterslip, suggested a lower likelihood for a large earthquake to occur in the SW shallow sector of the fault [16].

In this paper, we have analyzed Synthetic Aperture Radar (SAR) data in order to image the coseismic and post-seismic deformation of the Van earthquake, mapping also coseismic fractures and landslides. We have constrained the slip distribution on the main fault using Line Of Sight (LOS) and azimuth (\sim NS) components of ground displacement obtained from SAR data. We used a numerical fault modeling approach (by means of Finite Elements (FE)) in order to consider the elastic heterogeneities of the Van province. The 3D model was derived from tomography and receiver functions studies, and allowed us to investigate the possible structural control on the retrieved fault-slip source. We focused on the contribution of the ground deformation observations to the understanding of the main features of the Van earthquake sequence. Some of the SAR data employed in our work were previously published (e.g., [3,13–15]), but in this study we performed a detailed analysis of most of the available SAR data in order to give insights to the seismic hazard of the region despite non-optimal data coverage and coherence issues.

2. Tectonic Settings and Structural Data

The Anatolian plateau is geologically complex, and is dissected into numerous seismogenic faults. The compound lithospheric structure is accompanied by large seismic wave velocities variations, and the seismic activity is intense along highly heterogeneous zones (e.g., [17]). Unfortunately, little information is available at smaller scale, e.g., for the epicentral area of the Van earthquake. The Lake Van basin is located near the Karliova triple junction between the Anatolian microplate and the Eurasian and the Arabian plates, and this allowed materials upwelling from the Earth's mantle to accumulate in Lake Van and in the nearby volcanic area of Nemrut volcano [18]. Lake Van was the drill site of an International Continental scientific Drilling Program (ICDP) called PALEOVAN [19,20]. The seismic survey related to ICDP PALEOVAN revealed tephra deposits due to the historical activity of Nemrut volcano, and very localized features, such as clinofolds extending few hundreds of meters. However, the physical properties reported are related to very shallow depths, and therefore unable to characterize the whole seismogenic zone. Salah *et al.* [20] computed a 3D tomography of the crust beneath the eastern Anatolia (between latitudes 37.0° N– 41.0° N and longitudes 38.0° E– 44.5° E) from *P*-waves and *S*-waves (V_p and V_s , respectively). The Lake Van area is associated with a heterogeneous velocity structure. High V_p and V_s anomalies are constrained near the surface, while low velocity zones are widely present at 20–30 km depth. The Moho depth in the Van Province is estimated to be at 42–44 km depth [17]. The low velocity anomalies are interpreted as being caused by hot lithosphere resulting from the Arabian-European plates collision, while high V_p and low V_s (corresponding to a high Poisson ratio anomaly) imply the presence of fluids ascending upward from the hot lithosphere.

We took advantage from the numerical modeling approach to include in our models the elastic structure as imaged by the tomographic study [20]. In addition to these data, we considered V_s values in the epicentral area resulting from joint inversion of teleseismic receiver functions and surface waves by [17] at the stations VANB and CLDR.

3. Coseismic Ground Deformation and Modeling

3.1. Coseismic Geodetic Data

We processed a total of 32 SAR images (Table S1 in the Supplementary Data) from both X-Band (COSMO-SkyMed and CSK) and C-Band (ASAR ENVISAT, and ENV) satellites along the descending orbit using the software packages Sarscape [21] and Gamma [22]. Unfortunately, the ascending orbit data could not be considered since the first pre-seismic image was too far in time, *ca.* 3 years before the

mainshock, and was not suitable to produce coherent interferograms. It is also worth to mention that an ascending coseismic TERRASAR-X (TSX) pair exists [23], but it shows serious coherence issues due to the very large temporal baseline (pre-seismic image acquired on the 2009).

We adopted two different interferometric techniques to retrieve the coseismic displacement field, the classical Differential SAR Interferometry (InSAR) and Multi Aperture Interferometry (MAI) [24]. These techniques allow for the cross-validation of independent results, although with different spatial resolution and accuracy. The InSAR images were generated with 10 m pixel ground resolution for CSK (multilooking factor equal to 5 in azimuth and range) and 90 m for ENV (multilooking factor equal to 20 for the azimuth and 4 for the range), using a 30 m DEM from the ASTER mission to remove the topographic phase contribution and for geocoding. A set of ground control points was chosen from highly coherent regions located outside the high displacement area, in order to estimate and remove the contribution of orbital uncertainties. A filtering step was performed, based on the Goldstein algorithm [25]. Finally, the phase unwrapping was performed applying the Delauney minimum cost flow algorithm [26] to minimize possible phase jumps. The MAI analysis was carried out using a cross-correlation window size of 400 m \times 400 m. The characteristics of the coherent SAR interferograms are sketched in Figure 2 and listed in Table 1, while the measured coseismic displacement field is shown in Figure 3. The range measurements (CSK1, Figure 3a) cover a large part of the coseismic displacement field and show maximum LOS values of less than 1 m towards the satellite in the North, decreasing southwards. The azimuth measurements (Figure 3b) confirm the compressional kinematics (northern sector negative and southern sector positive) with extreme values located in the same area of the LOS highest values. The displacement maps obtained from the two ENV interferograms from adjacent tracks show very different coherence. The first one (ENV1, Figure 3c) captures the eastern part of the ground displacement with a good spatial coverage in spite of the large baselines (Figure S1), showing 44 cm maximum LOS displacement. The second interferogram is much less coherent (Figure S2). The phase unwrapping was very problematic and we eventually resolved to unwrap the clearest fringes using a manual procedure involving visual interpretation of the fringe continuity in three different areas of the image. The analysis was carried out given the important constraint provided by the coverage of the very near field coseismic area. This procedure generated ground displacement values (ENV2, Figure 3d) affected by a somewhat higher uncertainty, estimated as 1–2 fringe uncertainty. The superposition with CSK1 in the western part of the image was used to choose an offset for the unwrapped phase, and it was useful for a comparison.

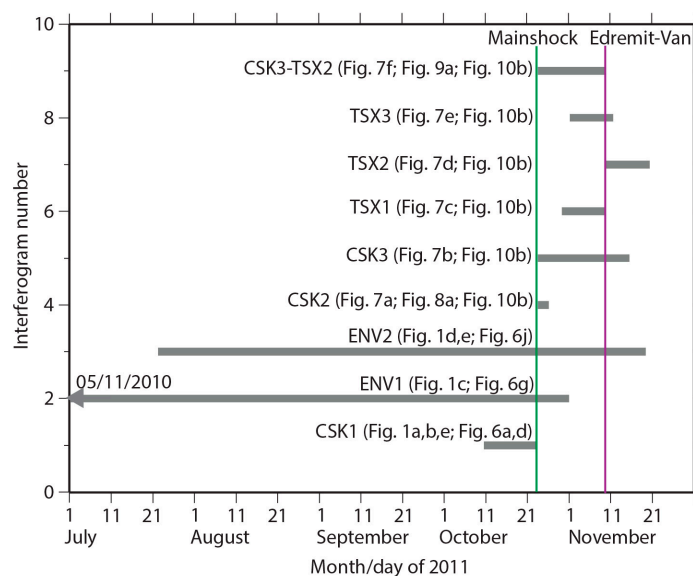


Figure 2. Graphical representation of the interferograms' time span during the coseismic and post-seismic phases.

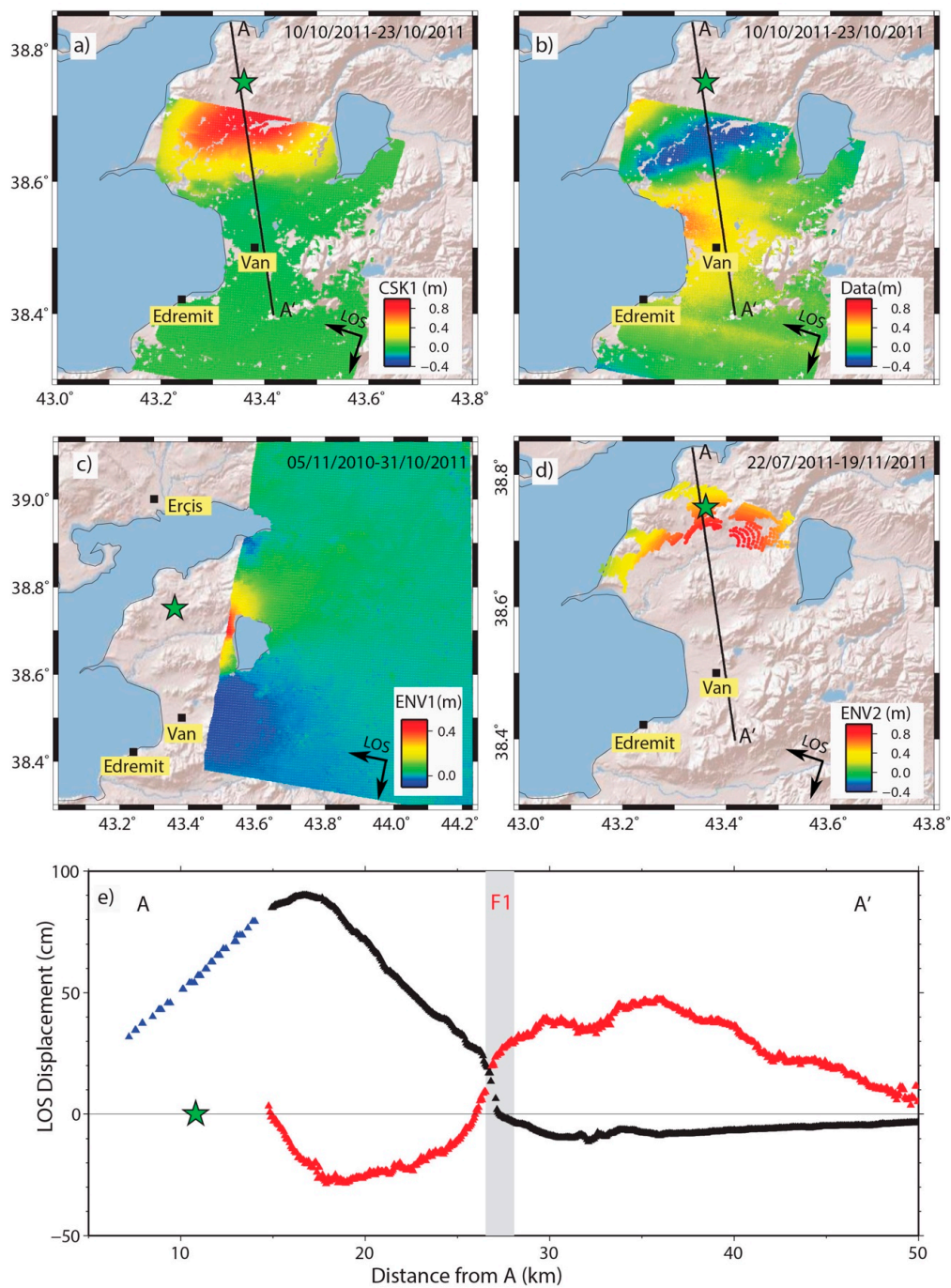


Figure 3. InSAR results: (a) CSK range results (*i.e.*, LOS direction); CSK1; (b) CSK azimuth results (positive Northwards); (c) ENV1, LOS displacements; and (d) ENV2, LOS displacements. SAR data details can be found in Table 1; (e) Data along the profile AA': CSK1 (range measurements, black), CSK (azimuth measurements, red), and ENV2 (LOS measurements, blue). The grey vertical band indicates the fault trace (F1) and its uncertainty (~1 km). The green star is the hypocenter.

Table 1. Characteristics of the interferograms used to map the coseismic and post-seismic phases.

Mission	Orbit	Acquisition Dates	Phase ^a	Perpendicular Baseline (m)	Temporal Baseline (days)	Incidence Angle (°)	Fringe Rate (cm)
COSMO-SkyMed (CSK1)	Descending	10 October 2011 23 October 2011	Co	192	13	29	1.6
ENVISAT (ENV1)	Descending	5 November 2010 31 November 2011	Co	633	360	41	2.8
ENVISAT (ENV2)	Descending	22 July 2011 19 November 2011	Co	270	120	41	2.8
COSMO-SkyMed (CSK2)	Descending	23 October 2011 26 October 2011	Post	307	3	29	1.6
COSMO-SkyMed (CSK3)	Descending	23 October 2011 15 November 2011	Post	79	23	29	1.6
Terrasar-X (TSX1)	Descending	29 October 2011 9 November 2011	Post	292.2	11	26.3	1.6
Terrasar-X (TSX2)	Descending	9 November 2011 20 November 2011	Post	11.5	11	26.3	1.6
Terrasar-X (TSX3)	Ascending	31 October 2011 11 November 2011	Post	190	11	33.2	1.6

^a Co is referred to the coseismic phase, Post is the post-seismic phase.

The profile AA' (Figure 3e), across the extreme LOS values and close to the epicenter, shows a continuous pattern of ENV2 and CSK1 datasets. The grey vertical band (F1) reports the fault trace position (within errors) resulting from our following geophysical inversion and corresponds to the steepest ground displacement gradient. Both the range and azimuth results from CSK show a compressive regime and a halfway discontinuity. The spatial continuity between the CSK1 and ENV1 unwrapped interferograms is shown in Figure S3.

3.2. Fractures and Landslides from InSAR Data

The Van earthquake caused some surface ruptures, mapped during field work and summarized by [7] and references therein. We analyzed the high resolution CSK wrapped InSAR image in order to identify phase jumps and fringe discontinuities corresponding to surface fractures. We distinguished two families of subparallel discontinuities ~ENE oriented and located at about 38.57°N (FA) and 38.64°N (FB), as shown in Figure 4. The group FA is approximately located along the surface projection of the mainshock fault plane, and it corresponds to the main surface rupture, approximately 8 km long, as described in [7]. Another fringe discontinuity group, FB, occurred close to the lobe of largest coseismic LOS deformation. These discontinuities are compatible with a set of probable ruptures related to secondary left-lateral strike-slip structures activated during the Van seismic sequence, as suggested by [7] and shown in their Figure 4.

Additional anomalous fringe patterns and/or decorrelation areas can be found in Figure 4A. Some of these patterns could be due to surface phenomena related to the earthquake occurrence, like landslides. Indeed, the coseismic shaking could activate landslides characterized by a deep or shallow rupture surface (e.g., [27] and references therein). By analyzing the CSK wrapped interferogram, we identified a landslide type called *Deep-seated Gravitational Slope Deformation* (DGSD), located about 43.5123°E, 38.6244°N (landslide 1 in Figure 4A–C). This type of phenomena is normally characterized by variable deformation rates from less than 1 mm to few centimeters per year, and they could be triggered by seismic events or heavy rainfall. Moreover, DGSDs are often revealed with geomorphological evidences, such as double crest ridges, counterscarps or gravitational half-grabens. Some of these features, such as crest ridges and counterscarps, were also recognized for the landslide

1 of this work. In the CSK interferogram, the area involved by the DGSD shows a different fringe pattern. In particular, the spacing between the fringes into the landslide body appears to be larger (and chaotic) with respect to the area nearby the landslide, where the fringe spacing is regular and follows the pattern due to the coseismic displacement (Figure 4B). This is also observable in the along-slope displacement profile (green stripe in Figure 4C) from the CSK unwrapped phase, where we observe the regular coseismic displacement distorted by a well-localized displacement pattern related to the coseismic activation of the DGSD. Indeed, the signal corresponds to the landslide body that moves downstream as an independent mass, and it is characterized by a different dislocation of the upper part of the landslide body with respect to the accumulation zone. In addition, North of landslide 1 there are three small areas where a loss of coherence occurs (Figure 4A,B). The regular fringe pattern is sharply interrupted in correspondence of these areas: this phenomenon could be associated to sudden motion temporally occurred between two SAR acquisitions. By comparing the InSAR fringes with optical imagery, we identify three landslides (labeled 2, 3 and 4 in Figure 4A,B,E) located near the epicenter area, suggesting the occurrence of additional coseismic displacement due to the seismic shaking.

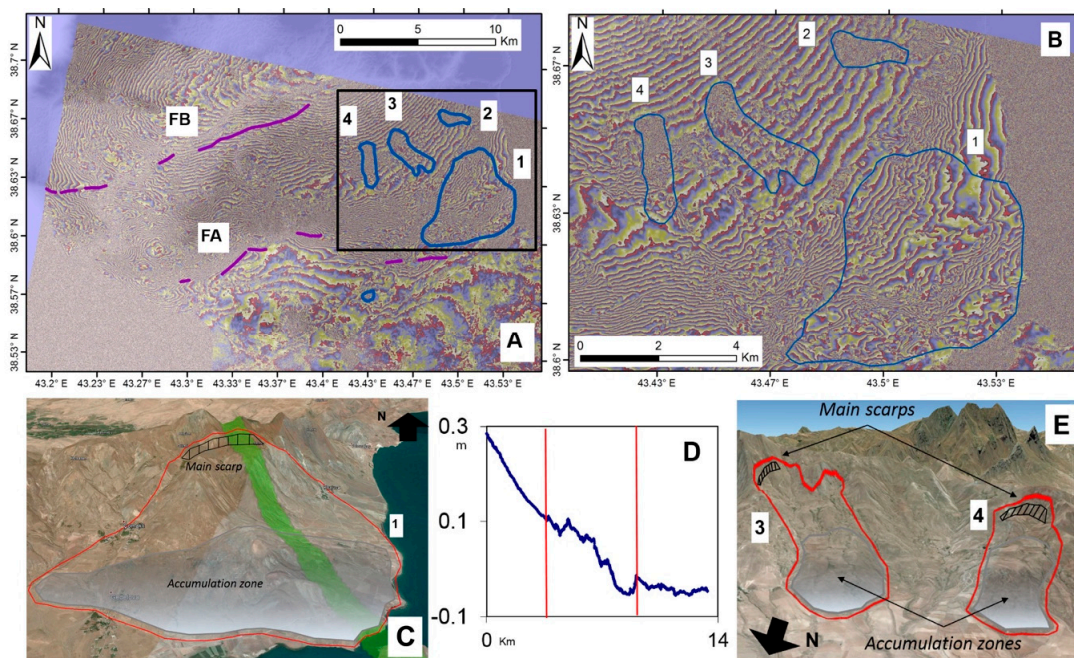


Figure 4. Fractures and landslides from InSAR: (A) wrapped phase of the CSK interferogram, where some crack lineaments (FA and FB, purple lines) and landslides (blue lines) are recognized; (B) zoomed view of the landslides; (C) Google Earth view from South of landslide 1 (red lines); and in green the displacement profile shown in (D), where the two red bars indicate the DGSD body; (E) Google Earth view from NNW of landslides 3 and 4, indicated in red.

3.3. Model of the Mainshock Source

The geodetic data collected were used to retrieve the coseismic slip distribution of the mainshock fault through an inversion procedure. We adopted a two-step inversion framework, initially optimizing the source parameters [28] using a non-linear inversion algorithm, followed by a Bayesian study on the inverted parameters (Neighborhood Algorithm (NA) [29,30]). This procedure settles the most probable ensemble of solutions, instead of a single best-fit model. In the second step, the defined fault plane is accepted for FE modeling with the commercial code [31]. The slip distribution was constrained through a linear inversion in the heterogeneous FE forward model, adopting a procedure already tested in seismic source inversions [32].

The SAR datasets were subsampled in a regular grid with a step of 1 km (except for ENV1, subsampled with a step increasing according with the epicentral distance), obtaining a total of 5314 data points. In addition to the SAR data, we considered the coseismic GPS data belonging to the Turkish CGPS network. The stations are spread in a region of 350 km \times 450 km, and only two stations (MURA and OZAL) out of 16 in total are included in the largest ENV1 frame, *i.e.*, within 50 km from the epicenter (Figure 1).

We carried out several tests during the non-linear inversions in order to balance the weight of the SAR and GPS data (e.g., [32]), and to limit the trade-offs among fault parameters (e.g., top left corner coordinates and strike, fault width and depth). In the preferred non-linear inversion configuration, the GPS misfit weighs 5% respect to the SAR misfit, due to the very high signal-to-error ratio of the GPS dataset and the presence of only two near-field GPS benchmarks. The fault width and dip were fixed at 18 km and 50°, respectively (e.g., [8,9]), and within the ranges proposed by [3,13]. Both the fault width and dip could be estimated from accurate aftershock locations in 3D, but even in the relocated catalogue from [2], the seismicity is too scattered for this purpose (Figure 5b). A down-dip rupture width of 20 km for a M 7.1 reverse slip earthquake was estimated [33].

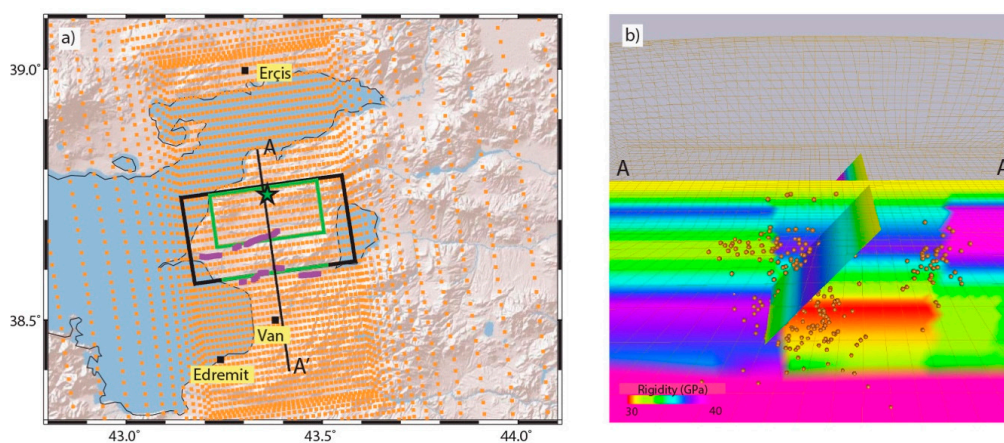


Figure 5. FE model of the Van Earthquake: (a) Top view of the model. The uniform slip fault is reported by green line while the fault plane used to retrieve the slip distribution is indicated by the black line. Surface ruptures constrained by InSAR are indicated by purple lines. The green star is the hypocenter and the orange dots are the surface nodes of the FE model; (b) Rigidity distribution on the section AA' (see Figure 3) and on the fault plane within the heterogeneous FE model, view from West. The external edges of the FE model are shown with ochre lines. The seismicity within few kilometers from the section is reported by ochre spheres.

The resulting values of the free parameters are reported in Table 2, while the Posterior Probability Density (PPD) functions are shown in Figures S4 and S5. The source parameters are well constrained since the PPDs have narrow bell-shaped distributions. The uncertainties of the obtained parameters are taken from the half-widths of the distributions themselves. The length ($L = 24$ km) is the worst constrained parameter and shows trade-offs with the Easting, Northing and slip of the fault. This is not surprising since minor variations of the fault position may be accommodated by small adjustments in the fault length and slip amount, in order to reproduce the surface displacement pattern. A minor trade-off between the strike angle and Northing is also to be mentioned. Data inversion shows that the thrust fault mechanism has a minor left-lateral component, being the rake equal to 72°, as expected from the focal mechanism (Figure 1). The fault trace, obtained extending the fault plane to the free surface, follows the surface fractures (Figure 5a) and corresponds to the displacement discontinuity shown in the profile in Figure 3e (fault F1). The computed scalar seismic moment is 5.5×10^{19} Nm, using a rigidity value of 35 GPa (average of fault rigidities depicted in Figure 5b), corresponding to Mw 7.1. The error associated to the scalar moment is estimated from its PPD distribution as 10%–15%

its mean value (Figure S5). All the source parameters constrained are in accordance, within their uncertainties, with previous findings, e.g., the InSAR inversions by [13]. Residuals are reported in Figures S6 and S7.

Table 2. Fault parameters retrieved by non-linear inversion.

Latitude ^{a,b}	Longitude ^{a,b}	Depth ^{a,b} (km)	Length ^b (km)	Width ^c (km)	Strike ^b (°)	Dip ^c (°)	Slip ^b (m)	Rake ^b (°)
38.676	43.506	8.7 ± 0.5	24.0 ± 1.1	18	263 ± 4	50	3.6 ± 0.5	72 ± 5

^a The fault position (latitude, longitude and depth) is referred to the top left corner; ^b The standard deviation of every parameter is estimated from the half-width of the PPD distributions (Figure S4). The standard deviations retrieved are 800 m for the latitude and 600 m for the longitude; ^c The parameter is fixed from literature (see text for details).

We then proceeded to constrain the slip distribution in a 3D numerical model, employing the fault geometry determined above. The fault dimensions were enlarged up to $L = 36$ km and width $W = 30$ km, maintaining the same dip, strike and trace center, and extending the plane till the surface. The 3D FE model is made of ~200,000 8-node brick elements (partial layout depicted in Figure 5). The whole FE cylindrical domain has a diameter of 440 km and height 170 km, to avoid undesirable boundary effects. The grid resolution is 1 km in the fault near field, and increases up to 10–20 km in the far field (bottom and edges). The fault plane is subdivided into patches of 2 km side. The elastic structure of the FE model was computed from the Vp and Vs data resulting from tomography [20] and receiver functions studies [17]. Although the tomography by [20] is one of the few tomographic studies of the region, it is rather coarse for our purpose since it is referred to a regional scale, with horizontal resolution of 20–30 km and layers at 4/12/25/40/55 km. The velocities were converted into elastic parameters using a density profile linearly increasing with depth, as the Vp increases, $\rho = 541 + 360Vp$ [34]. Each element of the grid was characterized by independent constants without layering approximation [32]. The FE domain assumed the following values: rigidity $20 \text{ GPa} < \mu < 63 \text{ GPa}$, Poisson coefficient $0.17 < \nu < 0.33$ and density $2400 \text{ kg/m}^3 < \rho < 3300 \text{ kg/m}^3$. The fault plane was characterized by a smaller variability of elastic constants: $30 \text{ GPa} < \mu < 40 \text{ GPa}$, $0.25 < \nu < 0.31$ and $2700 \text{ kg/m}^3 < \rho < 2900 \text{ kg/m}^3$. Similar results were also obtained along the AA' profile perpendicular to the fault strike (Figure 5b). Once the FE model was set up, elementary Green's Functions were computed by applying unitary slips on each patch separately, and the obtained surface displacements were recorded in a matrix. In this way, the slip distribution was optimized in the heterogeneous medium. The full procedure was described in [32], while the slip distribution was obtained through a linear inversion procedure based on the singular value decomposition (e.g., [35]). The slip uncertainty was calculated according to the standard rules for uncertainty propagation $\text{cov}_m = G^{-g} \text{cov}_d G^{-gT}$, where cov_m and cov_d are the variance/covariance matrices of the observed data and model parameters, respectively, and G^{-g} is the generalized inverse of the linear system. The standard deviation of the slip is the root of the cov_m diagonal values.

The slip distribution is characterized by a main zone of slip concentration expanding along strike between 12 km and 17 km depth (Figure 6a). The high slip zone is horizontally drop-shaped and extends up-dip from the hypocenter. It becomes thinner and shallower in the SW part of the fault. The maximum slip amounts to 8.4 m, and no significant slip is retrieved at shallow depths, above 7–9 km depth, in accordance with previous findings (e.g., [13]). The fractures of the group FB detected in Section 3.2 correspond to the vertical projection of the upper limit of the slip area in the SW part of the fault. The high slip gradients at the edges of this area may have concurred to the generation of these fractures. The errors associated to the slip distribution amount to few centimeters at shallow depths and increase up to more than 1 m at the fault bottom (Figure 6b). The area of high slip is characterized by uncertainties of 20–30 cm. The scalar seismic moment, determined by taking into account the actual rigidity associated to each patch within the FE model, is $5.0 \times 10^{19} \text{ Nm}$, equivalent to Mw 7.1.

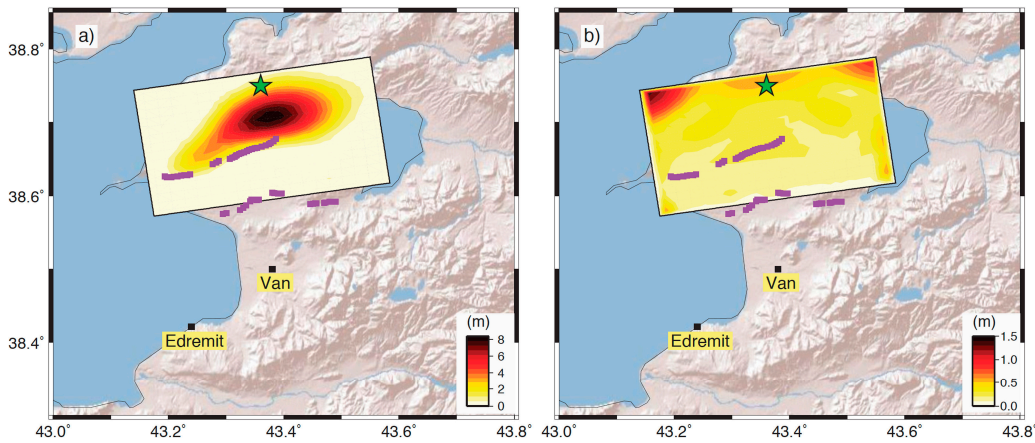


Figure 6. Fault slip distribution retrieved from geodetic data: (a) fault slip distribution; and (b) error associated. The surface fractures are reported by purple lines, and the Van earthquake epicenter by the green star.

Figure 7 shows comparisons between data and model. The datasets are rather heterogeneous, being composed by four coseismic displacement maps having different characteristics in terms of spatial coverage and associated errors, plus the GPS displacements. The whole pattern of the LOS displacements is generally reproduced and the agreement between data and model is within the related errors with percentages of 83.4% (CSK1), 99.8% (ENV1), and 95.6% (ENV2). Larger differences are observed between the azimuth direction data and model (71.9% of residuals are within errors) and GPS (only 52% within errors, full coverage residual map in Figure S8). The bad fit with GPS data is due to the regional scale of the GPS network, extending behind the coseismic far field, and their reduced weight in the misfit function. Even if positive residuals are found near Van, the NS data help to reduce the single orbit constraint of CSK1, ENV1 and ENV2. This is particularly compelling due to the specific fault orientation (~EW) of the Van earthquake fault.

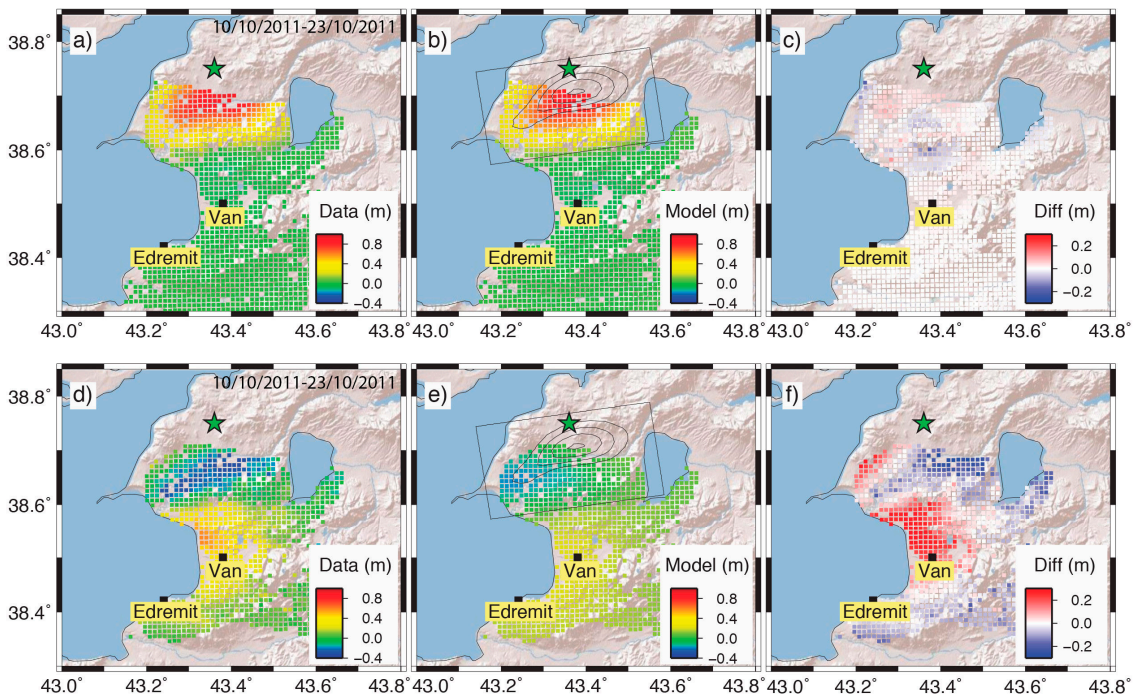


Figure 7. Cont.

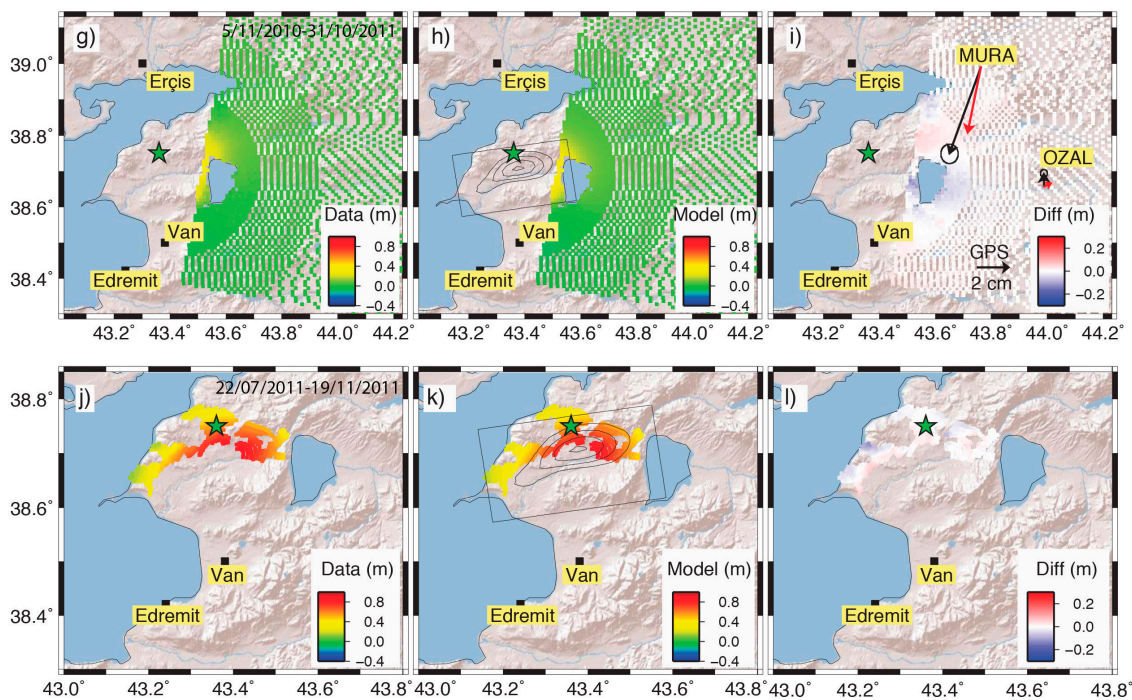


Figure 7. Comparisons between observed data (first column) and predictions (second column) related to the coseismic displacements of the Van earthquake. The residuals are observed minus modeled data (third column): (a–c) CSK1 (1210 data points); (d–f) CSK azimuth data (891 points); (g–i) ENV1 (2317 data points), near field GPS displacement vectors are also reported (black, observed; red, computed); and (j–l) ENV2 (896 data points). The green star is the hypocenter while the fault embedded in the FE model is indicated in black, with slip contour each 2 m.

4. Post-Seismic Ground Deformation and Modeling

4.1. Post-Seismic Geodetic Data

Table 1 and Figure 8 report the CSK and TSX image pairs used to measure the post-seismic displacements, selected from a larger number of images, including ENV (Table S1). We exploited the SAR dataset (Table S1) by computing several post-seismic pairs. Complete multi-temporal processing was not possible because of the low number of available acquisitions. The main problem with the post-seismic InSAR results was the interferograms' decorrelation due to the snow coverage and atmospheric effects. To reduce the influence of these limitations, we selected a CSK pair with a temporal baseline of only three days (and about 300 m for the normal baseline), whose master is 23 October 2011. In this way, we minimized the decorrelation contribution due to the temporal baseline. Moreover, we reduced the decorrelation noise by multilooking with a factor 11 in azimuth and in range, in order to get a pixel ground dimension of 25 m. Once the differential interferogram was computed, filtering and phase unwrapping were performed similarly to the coseismic data analysis. The obtained descending interferogram (CSK2, Figure 8a) shows a belt of positive values (up to 11 cm LOS) in the hanging wall, close to the fault trace. Some residuals due to atmospheric artifacts are present in the southern part of the interferogram, quite far from the high displacement area. Few centimeters of negative deformation are found in the northern part of the image. Another CSK interferogram is between the mainshock and 15 November 2011 (CSK3, Figure 8b), with longer temporal baseline and showing values up to 16 cm LOS. However, the Edremit-Van earthquake (9 November 2011) is included in this temporal span, and the displacement pattern located South of Van may be attributed to this Mw 5.7 event.

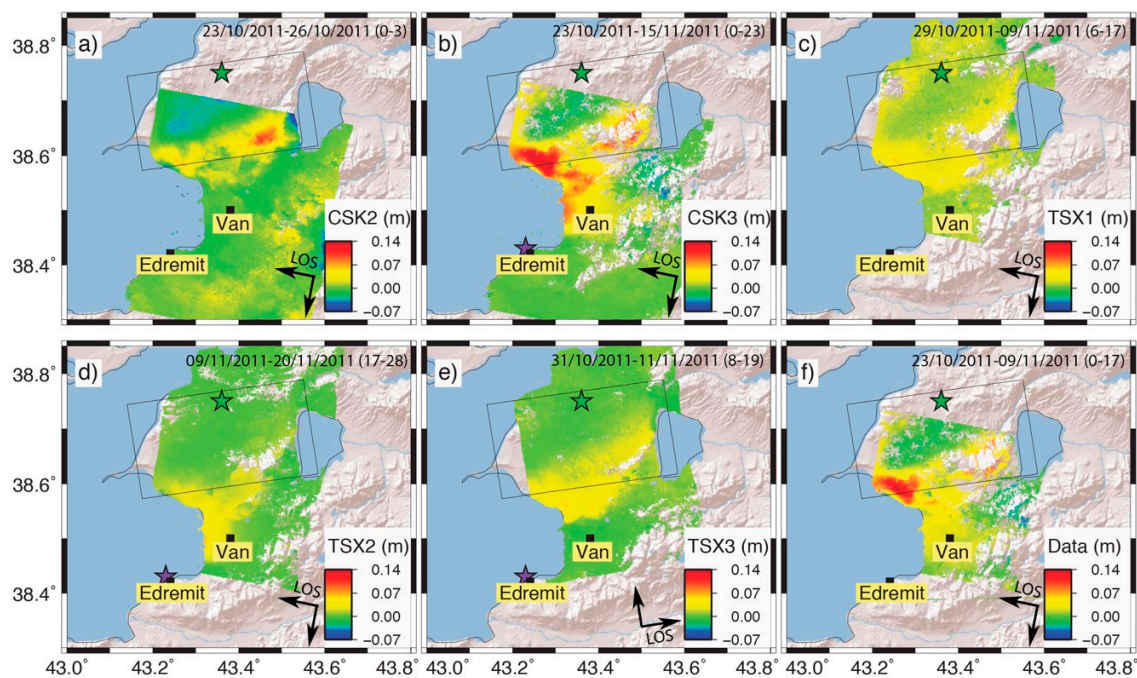


Figure 8. Post-seismic InSAR results from CSK and TSX satellites: (a) CSK2; (b) CSK3; (c) TSX1; (d) TSX2; (e) TSX3; and (f) difference between CSK3 and TSX2 (see text and Table 1 for details). Master/slave dates are indicated, along with the days after the mainshock in brackets. The green star is the mainshock epicenter and the purple star is the Edremit-Van earthquake epicenter (shown only if included in the temporal baseline).

From the exploitation of the TSX dataset, we obtained two descending orbit interferograms spanning from few days after the Van earthquake to few hours before the Edremit-Van earthquake (TSX1, Figure 8c) and from before the Edremit-Van earthquake to 20 November 2011 (TSX2, Figure 8d). We use the same multilook factor as CSK, 11, in range and azimuth. TSX1 shows a pattern similar to CSK2 and CSK3, with highest LOS displacements close to the shore of Lake Van, North of Van. The signal in TSX2 between Van and the shore may be associated to the displacement due to the Edremit-Van earthquake. Only one pair of ascending TSX images provided good results in terms of coherence (TSX3, Figure 8e). The map shows displacements strongly affected by both the post-seismic deformation of the Van earthquake and the deformations due to the Edremit-Van earthquake. As a final remark, we exclude that the observed signals are due to atmospheric artifacts since the post-seismic deformation is found in all the interferograms in Figure 8.

In order to obtain a better representation of the temporal evolution of the Van earthquake post-seismic deformation, we attempted to remove the geodetic signal of the Edremit-Van earthquake by subtracting the TSX2 displacements from the CSK3 displacements. The CSK3 image spans from the mainshock to 15 November 2011, while the TSX2 master image was acquired few hours before the Edremit-Van earthquake and the slave image is dated 20 November 2011. In this process we assumed that the CSK and TSX satellites had the same LOS (there are few degrees of difference in the looking angles) and that the five-day difference between the two slave images carried negligible post-seismic displacement. In this way, we obtained a map of 17-day displacements from the mainshock to the Edremit-Van earthquake, excluding the latter. The result, shown in Figure 8f, has an oblique belt of positive displacements near the fault trace, similarly to the three-day post-seismic interferogram CSK2, to TSX1 and to the original CSK3 (Figure 8a–c). High positive displacements are located close to the Lake Van shoreline, near the town of Bardakçı, for a maximum amount of 14 cm. The area corresponds to the place of surface ruptures as documented by [7], and confirmed by this work.

4.2. Afterslip Modeling

To study the post-seismic phase of the Van earthquake we assumed that the ground displacements were generated by the afterslip on the coseismic fault. The afterslip distributions are computed by means of the FE model adopted in the coseismic phase. The three-day afterslip constrained by CSK2 (Figure 9) shows a shallow distribution that extends from Lake Erçek, where it reaches ~30 cm, toward the WSW close to Lake Van. The high slip patch is shallow, between 1 km and 7 km, in opposition to the coseismic results in Figure 6. The slip distribution uncertainty is shown in Figure S9. The geodetic moment, computed using the actual rigidity values on the fault, amounts to 9.8×10^{17} Nm, corresponding to an equivalent Mw 5.9 (similarly to [13]). A band of positive residuals is found near and across the fault trace (Figure 9c), while in the northern area (hanging wall) the residuals are lower and negative. The residuals are at 78.9% within the data error (1.5 cm). These residuals may imply different fault geometry at shallow depths.

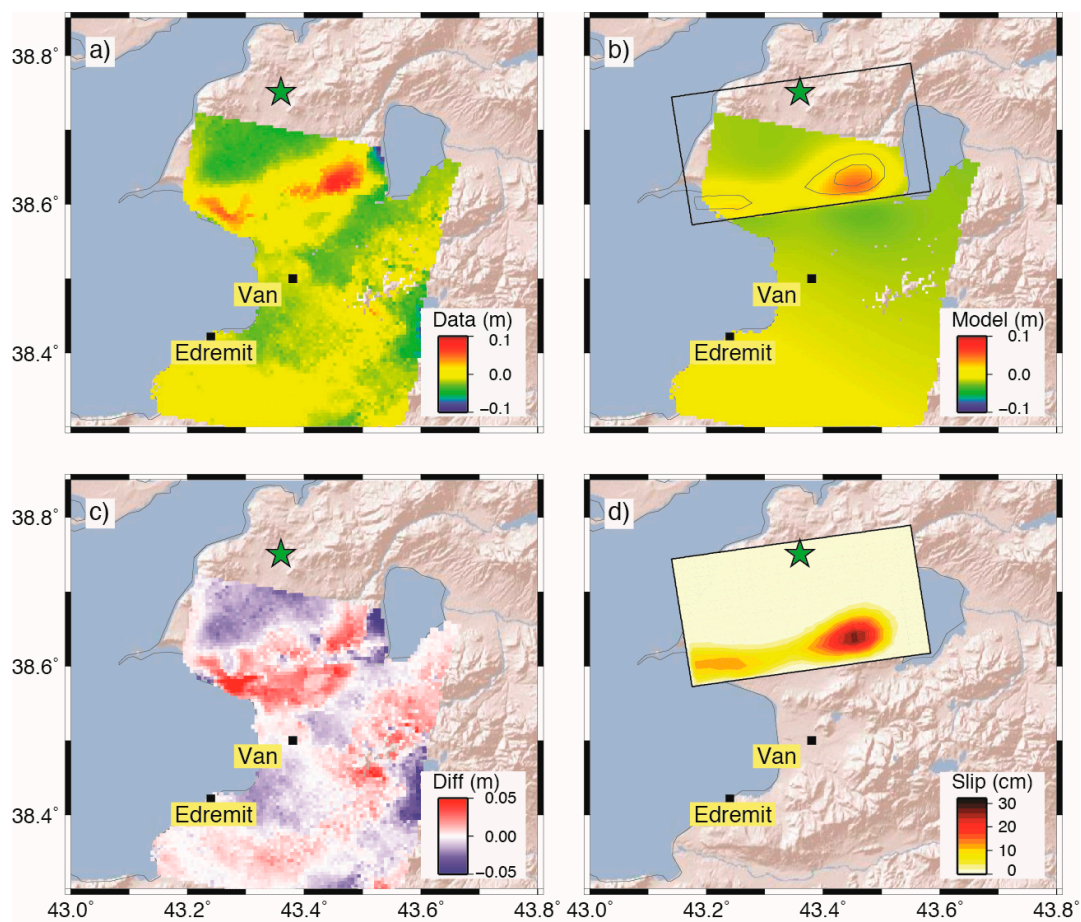


Figure 9. Post-seismic InSAR data and modeling (three-day temporal baseline): (a) subsampled CSK2 data (step of 500 m, 5660 data points); (b) modeled LOS displacements and the fault afterslip contour each 10 cm; (c) residuals (observed minus modeled data); and (d) related afterslip distribution. The green star is the mainshock epicenter.

Results from the afterslip computations related to the 17-day displacements are shown in Figure 10. The afterslip distribution shows two separate areas of slip concentration, both in the upper part of the fault, above 9 km depth. The larger one is located in the eastern part of the fault, and broadens the slip pattern already found in the first three days, reaching about 40 cm of slip. The second is located in the very shallow fault, at 3–4 km depth in the western sector of the fault, close to Lake Van. Data and model show quite similar patterns, but an area of positive residuals is found between Bardakçı and

Van. Unfortunately, the inverted data have low coherence in the high slip area (due to loss of coherence of both satellites from which it is computed), where higher values were expected, according to the inferred slip. The residuals are at 88.6% within data errors, considering a larger error (3 cm) due to the procedure used to isolate the displacement for the 17-day temporal baseline. The computed geodetic moment in the FE heterogeneous medium is 1.6×10^{18} Nm, corresponding to Mw 6.1. The three- and 17-day post-seismic energy releases amount to 1/50 and 1/30 of the coseismic energy release, respectively. From the total energy released in 17 days post mainshock, ~60% was released in the first three days. A further aseismic release of $\sim 10^{19}$ Nm (equivalent to Mw 6.6) from the end of November 2011 for 1.5 years was computed [16].

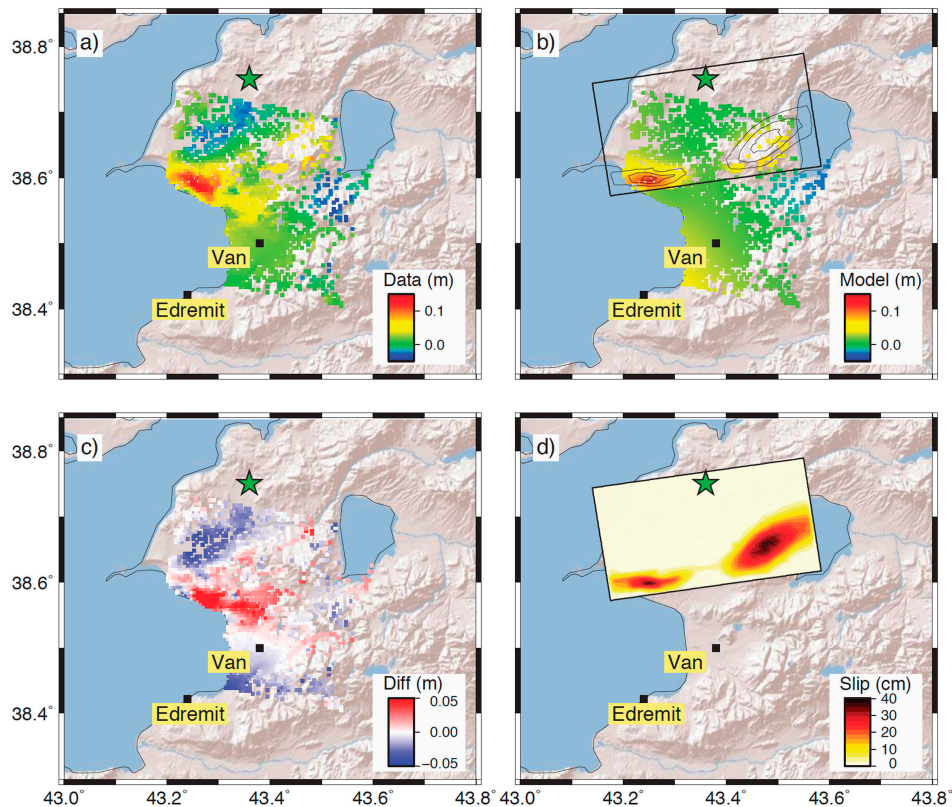


Figure 10. Post-seismic InSAR data and modeling (17-days temporal baseline): (a) subsampled data (step of 500 m, 1590 data points) computed from the difference between images CSK3 and TSX2 (see text for details); (b) modeled LOS displacements and the fault afterslip contour each 10 cm; (c) residuals (observed minus modeled data); and (d) related afterslip distribution. The green star is the mainshock epicenter.

5. Discussion

5.1. The 9 November 2011 Edremit-Van Earthquake

The Mw 5.7 Edremit-Van earthquake occurred offshore the town of Edremit, 15 km SW of Van. This event caused 40 fatalities and further collapse of tens of already damaged buildings. The earthquake, similarly to the event of 23 October 2011, took place on a fault that was not previously mapped (e.g., [4]). This second mainshock originated a sequence with a M 5.0 aftershock on 30 November 2011. The Edremit-Van earthquake had a dominantly dextral strike-slip focal mechanism (Figure 1). The conjugate planes' ambiguity (~EW and ~NS oriented) was discussed by various authors [2,10,12,15], generally endorsing the North dipping EW orientation, similarly to the mainshock fault [36]. Furthermore, the aftershocks of the Edremit-Van earthquake were fairly distributed with EW trend (Figure 1). The observation of the combined patterns due to different SAR orbits (TSX2,

Figure 8d and TSX3, Figure 8e) contributes to resolve the ambiguity, supporting the EW orientation hypothesis. Indeed, despite the ascending displacements (TSX3) includes part of the post-seismic data of the mainshock, they show opposite patterns South of Van, confirming the ~EW dextral mechanism (Figure 8 and profiles in Figure S10). The hypothesis of a NS strike slip fault at the epicenter longitude would provide negligible displacement in this area.

The role of the 23 October earthquake in promoting the Edremit-Van earthquake of 9 November was debated, discussing whether the latter is an aftershock of the mainshock or not. Computations of the changes in Coulomb stress (Coulomb Failure Function, CFF, e.g., [37]) endorsed the active role of the Van earthquake in promoting the Edremit-Van earthquake [12,15]. We simulated the variation of CFF projected on the presumed Edremit-Van fault (oriented EW at Lat. 38.45°N and extending 8 km × 5.75 km, [33]), by taking into account the coseismic and post-seismic slip distributions (Figure S11a). The whole Edremit-Van fault plane undergoes an increment of the CFF, supporting the possibility that the Van mainshock may have promoted the earthquake of 9 November 2011.

5.2. Geophysical Insights and Hazard Implications from SAR Analysis

From the comparison between slip and rigidity distributions (Figure 11), we observe that the high coseismic slip area expands from the hypocenter towards depths with higher rigidity. This is in accordance with previous findings (e.g., [32,38]), since the slip concentrates in asperities zones. However, in this case the rigidity shows long wavelength variations of only 22% along the fault plane and the tomographic data is too coarse compared to the fault dimensions to quantitatively affect the retrieved slip distribution. On the other side, good resolution structural data often evidence strong heterogeneities at the fault scale, with short wavelength variations that impact on the obtained slip distributions, either in case of continental earthquakes of moderate magnitude [32] or megathrust events [38]. As a final remark, we may also notice that the aftershocks are not particularly dense in the area of high coseismic and post-seismic slip but concentrate on the edges and on the bottom of the coseismic slip.

The coseismic slip distribution shows a large concentration area at hypocentral depths (12–17 km) with highest peak at about 14 km depth (Figure 11), and the rupture reaches only the depth of 8–10 km. These results are common to other authors [11,13,15]. Based on similar coseismic results, it was argued by [13] that the change of the Coulomb stress brought the upper, un-ruptured part of the fault closer to failure. Our post-seismic data and modeling show that the shallow section of the fault underwent considerable aseismic slip during the early days after the mainshock. Yet during the first 3 days after the mainshock we retrieved few dozens of centimeters of afterslip in the upper part of the fault close to Lake Erçek. During the following weeks, the slip has continued to increase in the same area, and a slip concentration patch appeared close to the western corner of the fault, near the Lake Van shore. Therefore, we argue that all the upper part of the fault accommodated aseismic slip. The shallow aseismic slip has continued also for the following 1.5 years, based on GPS data [16]. The afterslip in the upper section of the fault released an equivalent Mw 6.1 in the first 17 days after the mainshock and a further Mw 6.6 in the following 1.5 years (computed from the end of November 2011). This partially compensate the shallow slip deficit observed right after the mainshock, and overall, our results show the lowering of the seismogenic potential within the first 8–10 km of the fault through the release of a significant amount of energy during the post-seismic phase. We have also shown that shallow afterslip occurred along the full length of the fault and not only in the western sector as suggested by [16], whose results were probably biased by the partial coverage of the GPS network in the area near Lake Erçek, and by [13,14] using the three-day post-seismic image CSK2.

We simulated the variation of CFF by taking into account the coseismic and post-seismic slip distributions. The Coulomb stress change within the first 10 km of the fault observed in section AA' (e.g., Figure 3) results to be positive (*i.e.*, earthquake occurrence enhanced), even including the post-seismic afterslip (Figure S11b). This is due to the difference of one order of magnitude between the coseismic and post-seismic scalar moments, which implies that the stress drop due to the aseismic

slip cannot shadow the positive coseismic stress changes. However, we may account for several factors that may contribute to reduce the seismic hazard at shallow depths. As an example, the velocity strengthening characteristics of the shallow crust promotes faster falloff of slip velocity behind the rupture front and a decrease of slip towards the free surface (e.g., [39]). Therefore, limited slips are expected in the first kilometers below the free surface, further reducing the seismic potential. In our computations the shallow velocity strengthening characteristics, as feasible for the entire area east of Lake Van consisting of accretionary complex materials [40], are not taken into account. Furthermore, other post-seismic mechanisms such as viscoelastic and poroelastic behaviors may contribute to the post-seismic response, reducing the seismic hazard of that sector. Unfortunately, there is no detailed knowledge of the local structure and these possibilities cannot be fully investigated.

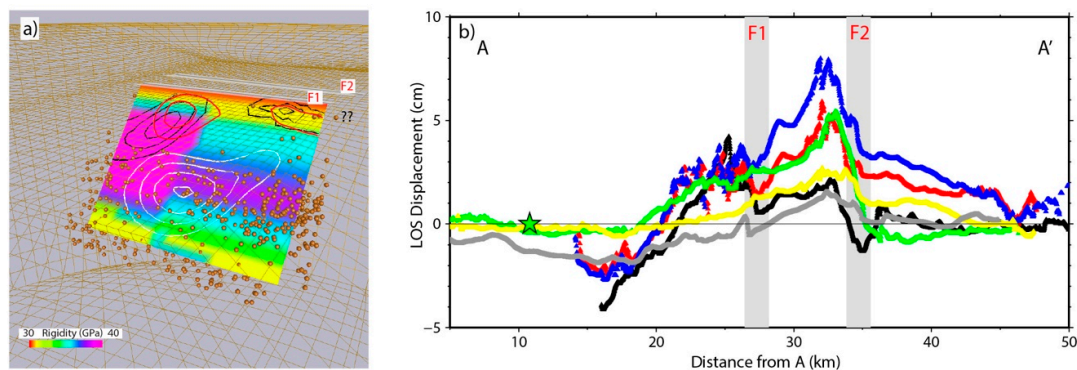


Figure 11. Coseismic and post-seismic results: (a) 3D view of the Van earthquake fault from the NW. Coseismic slip (white lines, contour every 2 m) and the post-seismic slip (red and black lines are three and 17 days after the mainshock, respectively, contour every 10 cm) superimposed on the rigidity heterogeneities of the fault plane within the FE model. Aftershocks hypocenters within 4 km from the fault are shown by ochre spheres; (b) AA' profile (see Figure 5a) across the traces of the main fault (F1) and the splay fault (F2). The colors are: CSK2, black; CSK3, blue; TSX1, grey; TSX2, yellow; TSX3, green; and the difference between CSK3 and TSX2, red. The green star is the Van earthquake epicenter.

We adopted only one fault in our inversions. Elliott *et al.* [13] resolved the slip on a pair of en echelon fault planes, based on the local morphology and the fault strike detectable in the CSK coseismic interferogram (Figure 4a). Their slip distribution shows two lobes, one on each fault, decreasing at the central border due to the sharp change of the fault dip. The existence of a reactivated aseismic fault, constrained by the GPS post-seismic data, was supposed [16]. Such splay fault extends from the western edge to the middle of the coseismic fault trace, shifted 7–8 km to the South. This secondary fault is supposed to join the main rupture at about 500 m below the surface, and using only GPS data the afterslip is found to be distributed both on the main and splay faults [16]. As mentioned above, even the relocated aftershocks [2] are too scattered and cannot be used to visualize more detailed features such as main fault segmentation and/or splay faults, especially those very shallow. Field observations and InSAR fringe patterns do identify minor surface fractures, as it occurs in many earthquakes but their direct relation to the mainshock rupture is far from clear. To better understand the InSAR contribution to the presence of the splay fault, Figure 11b reports all the post-seismic InSAR data along the AA' profile (as shown in Figure 3), where F2 is the trace of the presumed splay fault (as depicted by [16]) with ± 1 km uncertainty. Most of the patterns show a high gradient close to F2. This secondary plane seems actually to cause a discontinuity on the surface displacements, but nor the seismicity and other geophysical data constrain its depth. Given the limited independent knowledge about the local fault system, we did not attempt to set up inversions of complex faults (*i.e.*, double and/or listric faults), and eventually we adopted a single fault plane.

6. Conclusions

We have analyzed a large dataset of SAR images in order to study the coseismic and post-seismic phases of the Van earthquake sequence. Only few good quality interferograms resulted to be fruitful to constrain the slip distributions. Following the approach outlined in [32], we built a FE model of the Van earthquake that includes the structural information of the Van region. We computed coseismic and post-seismic slip distributions from the numerical model-based inversions.

We have here attempted to improve previous findings (e.g., [3,13–15]) employing most of the available geodetic data (InSAR and GPS) to constrain the slip characteristics of the Van Earthquake. Our approach, along with the employment of new-generation FE models, was aimed to contribute to the knowledge of the seismic hazard of the region. Our method allowed us to disclose further characteristics of the Van sequence, and to provide new insights for the regional/local risk assessment. The main new outcomes of our study are that the shallow part of the fault (above 7–9 km depth), unruptured during the coseismic phase, underwent afterslip in the post-seismic phase that may have reduced the seismic potential in its whole length from NW to SE. Furthermore, from the analysis of the InSAR data we were able to discuss the existence of a reactivated aseismic fault, that actually caused a discontinuity in the SAR profiles, previously hypothesized by means of few GPS [16].

As a conclusive remark, despite non-optimal data coverage (only single-orbit good-quality data available in the coseismic phase and for which coherence issues in the X-band post-seismic phase prevented the use of time series processing), we demonstrated that useful information could still be retrieved from SAR data through a detailed analysis.

Supplementary Materials: The following are available online at www.mdpi.com/2072-4292/8/6/532/s1. Figures S1 and S2: Wrapped InSAR images from ENVISAT satellite, Figure S3: Unwrapped adjacent coseismic InSAR data, Figure S4: PPD functions obtained from the non-linear fault inversion, Figure S5: Two-dimensional PPD distributions, Figure S6: Comparisons between observed and computed data of the coseismic displacements in the non-linear inversion, Figure S7: Full-scale map with GPS as computed in the non-linear inversion, Figure S8: Full-scale map with GPS as computed in the linear inversion, Figure S9: slip uncertainty distributions for the post-seismic analysis, Figure S10: Profiles of the InSAR data across the faults, Figure S11: CFF computations for the Edremit-Van earthquake, Table S1: Characteristics of all the SAR images acquired.

Acknowledgments: TERRASAR-X images and GPS data are available through the Group on Earth Observations (GEO) Geohazard Supersite initiative (<http://www.earthobservations.org/gsnl.php>). R. Cakmak (TUBITAK MRC EMSI) is acknowledged for the GPS coseismic field. ENVISAT data were provided by the European Space Agency (ESA) in the framework of the Category-1 project n. 5605. COSMO-SkyMed data were provided by the Italian Space Agency (ASI) in the framework of the SiGRiS project (ASI n. I/024/07/0), that partially funded this work. This work was also partially funded by the EU's H2020 EVER-EST Project (grant agreement 674906). We thank J. P. Merryman Boncori for taking part to the COSMO-SkyMed data processing. P. De Gori provided the relocated seismicity and M.K. Salah the tomographic data. A. Akinci and A. Antonioli are acknowledged for useful discussions. We thank three anonymous referees that helped us to improve the first version of this manuscript. The figures were generated using the commercial softwares ArcGis 10.0, Amira 5.4 and the open source software GMT (<http://gmt.soest.hawaii.edu/>).

Author Contributions: All the coauthors conceived and designed the present study. C.T. processed the InSAR data; G.P. worked on the fractures and landslides; E.T. performed the modeling and inversions; S.A. wrote the codes for linear inversions; and E.T., C.T. and G.P. wrote the paper.

Conflicts of Interest: The authors declare no conflict of interest.

References

1. Örgülü, G.; Aktar, M.; Türkelli, N.; Sandvol, E.; Barazangi, M. Contribution to the seismotectonics of eastern turkey from moderate and small size events. *Geophys. Res. Lett.* **2003**, *30*. [[CrossRef](#)]
2. De Gori, P.; Akinci, A.; Lucente, F.P.; Kılıç, T. Spatial and temporal variations of aftershock activity of the 23 October 2011 mw 7.1 Van, Turkey, earthquake. *B Seismol. Soc. Am.* **2014**, *104*, 913–930. [[CrossRef](#)]
3. Fielding, E.J.; Lundgren, P.R.; Taymaz, T.; Yolsal-Cevikbilen, S.; Owen, S.E. Fault-slip source models for the 2011 m 7.1 van earthquake in Turkey from sar interferometry, pixel offset tracking, gps, and seismic waveform analysis. *Seismol. Res. Lett.* **2013**, *84*, 579–593. [[CrossRef](#)]

4. Şaroğlu, F.; Emre, Ö.; Kuşçu, I. *Active Fault Map of Turkey, 1:2,000,000 Scale*; General Directorate of Mineral Research and Exploration: Ankara, Turkey, 1992.
5. Emre, Ö.; Duman, T.Y.; Özalp, S.; Elmaci, H.; Olgun, Ş.; Şaroğlu, F. *Active Fault Map of Turkey with an Explanatory Text, 1:250,000 Scale*; General Directorate of Mineral Research and Exploration: Ankara, Turkey, 2013.
6. Cetin, K.O.; Turkoglu, M.; Ünsal Oral, S.; Nacar, U. Van-Tabanlı Earthquake (mw = 7.1) 23 October 2011 Preliminary Reconnaissance Report. Available online: supersites.earthobservations.org/Van_EQ_Preliminary_Report_KOC.pdf (accessed on 15 March 2012).
7. Doğan, B.; Karakaş, A. Geometry of co-seismic surface ruptures and tectonic meaning of the 23 October 2011 mw 7.1 Van earthquake (east anatolian region, Turkey). *J. Struct. Geol.* **2013**, *46*, 99–114. [[CrossRef](#)]
8. Hayes, G. USGS. Available online: earthquake.usgs.gov/earthquakes/eqinthenews/2011/usb0006bqc/finite_fault.php (accessed on 25 October 2011).
9. Irmak, T.S.; Doğan, B.; Karakaş, A. Source mechanism of the 23 October, 2011, Van (Turkey) earthquake (m-w = 7.1) and aftershocks with its tectonic implications. *Earth Planets Space* **2012**, *64*, 991–1003. [[CrossRef](#)]
10. Utkucu, M. 23 October 2011 Van, eastern anatolia, earthquake (mw 7.1) and seismotectonics of lake van area. *J. Seismol.* **2013**, *17*, 783–805. [[CrossRef](#)]
11. Gallovič, F.; Ameri, G.; Zahradník, J.; Janský, J.; Plicka, V.; Sokos, E.; Askan, A.; Pakzad, M. Fault process and broadband ground-motion simulations of the 23 October 2011 Van (eastern turkey) earthquake. *B Seismol. Soc. Am.* **2013**, *103*, 3164–3178. [[CrossRef](#)]
12. Akinci, A.; Antonioli, A. Observations and stochastic modelling of strong ground motions for the 2011 October 23 m-w 7.1 Van, Turkey, earthquake. *Geophys. J. Int.* **2013**, *192*, 1217–1239. [[CrossRef](#)]
13. Elliott, J.R.; Copley, A.C.; Holley, R.; Scharer, K.; Parsons, B. The 2011 mw 7.1 Van (eastern Turkey) earthquake. *J. Geophys. Res. Sol.* **2013**, *118*, 1619–1637. [[CrossRef](#)]
14. Feng, W.P.; Li, Z.H.; Hoey, T.; Zhang, Y.; Wang, R.J.; Samsonov, S.; Li, Y.S.; Xu, Z.H. Patterns and mechanisms of coseismic and postseismic slips of the 2011 m-w 7.1 Van (Turkey) earthquake revealed by multi-platform synthetic aperture radar interferometry. *Tectonophysics* **2014**, *632*, 188–198. [[CrossRef](#)]
15. Moro, M.; Cannelli, V.; Chini, M.; Bignami, C.; Melini, D.; Stramondo, S.; Saroli, M.; Picchiani, M.; Kyriakopoulos, C.; Brunori, C.A. The 23 October 2011, Van (Turkey) earthquake and its relationship with neighbouring structures. *Sci. Rep.* **2014**, *4*. [[CrossRef](#)] [[PubMed](#)]
16. Dogan, U.; Demir, D.Ö.; Çakir, Z.; Ergintav, S.; Ozener, H.; Akoğlu, A.M.; Nalbant, S.S.; Reilinger, R. Postseismic deformation following the mw 7.2, 23 October 2011 Van earthquake (Turkey): Evidence for aseismic fault reactivation. *Geophys. Res. Lett.* **2014**, *41*, 2334–2341. [[CrossRef](#)]
17. Gök, R.; Mellors, R.J.; Sandvol, E.; Pasyanos, M.; Hauk, T.; Takedatsu, R.; Yetirmishli, G.; Teoman, U.; Turkelli, N.; Godoladze, T.; *et al.* Lithospheric velocity structure of the anatolian plateau-caucasus-caspian region. *J. Geophys. Res. Sol.* **2011**, *116*. [[CrossRef](#)]
18. Kipfer, R.; Aeschbachhertig, W.; Baur, H.; Hofer, M.; Imboden, D.M.; Signer, P. Injection of mantle type helium into lake Van (Turkey)—The clue for quantifying deep-water renewal. *Earth Planet. Sci. Lett.* **1994**, *125*, 357–370. [[CrossRef](#)]
19. Litt, T.; Krastel, S.; Sturm, M.; Kipfer, R.; Örcen, S.; Heumann, G.; Franz, S.O.; Ülgen, U.B.; Niessen, F. 'Paleovan', international continental scientific drilling program (ICDP): Site survey results and perspectives. *Quaternary Sci. Rev.* **2009**, *28*, 1555–1567. [[CrossRef](#)]
20. Salah, M.K.; Sahin, Ş.; Aydın, U. Seismic velocity and poisson's ratio tomography of the crust beneath east anatolia. *J. Asian Earth Sci.* **2011**, *40*, 746–761. [[CrossRef](#)]
21. Sarscape Sarmap sa, 5.0. Available online: <http://www.sarmap.ch> (accessed on 25 March 2013).
22. Werner, C.; Wegmüller, U.; Strozzi, T.; Wiesmann, A. Interferometric point target analysis for deformation mapping. *Geosci. Remote Sens. Symp.* **2003**, *7*, 4362–4364.
23. Wang, T.; Jonsson, S. Improved sar amplitude image offset measurements for deriving three-dimensional coseismic displacements. *IEEE J. Stars* **2015**, *8*, 3271–3278. [[CrossRef](#)]
24. Bechor, N.B.D.; Zebker, H.A. Measuring two-dimensional movements using a single insar pair. *Geophys. Res. Lett.* **2006**, *33*. [[CrossRef](#)]
25. Goldstein, R.M.; Werner, C.L. Radar interferogram filtering for geophysical applications. *Geophys. Res. Lett.* **1998**, *25*, 4035–4038. [[CrossRef](#)]

26. Costantini, M. A novel phase unwrapping method based on a network programming. *Geosci. Remote Sens. IEEE Trans.* **1998**, *36*, 813–821. [[CrossRef](#)]
27. Jibson, R.W. Methods for assessing the stability of slopes during earthquakes—a retrospective. *Eng. Geol.* **2011**, *122*, 43–50. [[CrossRef](#)]
28. Okada, Y. Internal deformation due to shear and tensile faults in a half-space. *B Seismol. Soc. Am.* **1992**, *82*, 1018–1040.
29. Sambridge, M. Geophysical inversion with a neighbourhood algorithm—II. Appraising the ensemble. *Geophys. J. Int.* **1999**, *138*, 727–746. [[CrossRef](#)]
30. Sambridge, M. Geophysical inversion with a neighbourhood algorithm—I. Searching a parameter space. *Geophys. J. Int.* **1999**, *138*, 479–494. [[CrossRef](#)]
31. Abaqus Dassault Systèmes Simulia Corp. Providence, 6.11. Available online: www.simulia.com (accessed on 1 February 2012).
32. Trasatti, E.; Kyriakopoulos, C.; Chini, M. Finite element inversion of dinstar data from the mw 6.3 l’aquila earthquake, 2009 (Italy). *Geophys. Res. Lett.* **2011**, *38*. [[CrossRef](#)]
33. Wells, D.L.; Coppersmith, K.J. New empirical relationships among magnitude, rupture length, rupture width, rupture area, and surface displacement. *B Seismol. Soc. Am.* **1994**, *84*, 974–1002.
34. Christensen, N.I.; Mooney, W.D. Seismic velocity structure and composition of the continental-crust—A global view. *J. Geophys. Res. Sol.* **1995**, *100*, 9761–9788. [[CrossRef](#)]
35. Atzori, S.; Hunstad, I.; Chini, M.; Salvi, S.; Tolomei, C.; Bignami, C.; Stramondo, S.; Trasatti, E.; Antonioli, A.; Boschi, E. Finite fault inversion of dinstar coseismic displacement of the 2009 l’aquila earthquake (central Italy). *Geophys. Res. Lett.* **2009**, *36*. [[CrossRef](#)]
36. Görgün, E. The 23 October 2011 m-w 7.2 Van-ercis, Turkey, earthquake and its aftershocks. *Geophys. J. Int.* **2013**, *195*, 1052–1067. [[CrossRef](#)]
37. Harris, R.A. Introduction to special section: Stress triggers, stress shadows, and implications for seismic hazard. *J. Geophys. Res. Sol.* **1998**, *103*, 24347–24358. [[CrossRef](#)]
38. Romano, F.; Trasatti, E.; Lorito, S.; Piromallo, C.; Piatanesi, A.; Ito, Y.; Zhao, D.; Hirata, K.; Lanucara, P.; Cocco, M. Structural control on the tohoku earthquake rupture process investigated by 3d fem, tsunami and geodetic data. *Sci. Rep.* **2014**, *4*. [[CrossRef](#)] [[PubMed](#)]
39. Kaneko, Y.; Lapusta, N.; Ampuero, J.P. Spectral element modeling of spontaneous earthquake rupture on rate and state faults: Effect of velocity-strengthening friction at shallow depths. *J. Geophys. Res. Sol.* **2008**, *113*. [[CrossRef](#)]
40. Şengör, A.M.C.; Özeren, M.S.; Keskin, M.; Sakıncı, M.; Özbakır, A.D.; Kayan, İ. Eastern turkish high plateau as a small turkic-type orogen: Implications for post-collisional crust-forming processes in Turkic-type orogens. *Earth Sci. Rev.* **2008**, *90*, 1–48. [[CrossRef](#)]

